Data-Augmented Matched Subspace Detector for Hyperspectral Subpixel Target Detection

Xiaochen Yang[a], Mingzhi Dong[a], Ziyu Wang[a], Lianru Gao[b], Lefei Zhang[c], Jing-Hao Xue[a,*]

[a]*Department of Statistical Science, University College London, London WC1E 6BT, U.K.*
[b]*Key Laboratory of Digital Earth Science, Institute of Remote Sensing and Digital Earth, Chinese Academy of Sciences, Beijing 100094, China*
[c]*School of Computer Science, Wuhan University, Wuhan 430072, China*

Abstract

The performance of subspace-based methods such as matched subspace detector (MSD) and MSD with interaction effects (MSDinter) heavily depends on the background subspace and the target subspace. Nonetheless, constructing a representative target subspace is challenging due to the limited availability of target spectra in a collected hyperspectral image. In this paper, we propose two new hyperspectral target detection methods termed data-augmented MSD (DAMSD) and data-augmented MSDinter (DAMSDI) that can effectively solve the scarcity problem of target spectra and from which a representative target-background mixed subspace can be learned. We first synthesise target-background mixed spectra based on classical hyperspectral mixing models and then learn a target-background mixed subspace via principal component analysis. Compared with MSD and MSDinter, the learned mixed subspace is more representative as spectral variability of target spectra is explained to the largest extent and it leads to an improvement in computational speed and numerical stability. We demonstrate the efficacy of DAMSD and DAMSDI for subpixel target detection on two public hyperspectral image datasets.

Keywords: Hyperspectral imaging, Matched subspace detector (MSD), Subpixel target detection, Data augmentation

*Corresponding author: Tel.: +44-207-679-1863
Email address: jinghao.xue@ucl.ac.uk (Jing-Hao Xue)

1. Introduction

Hyperspectral remote sensing collects the spectra for all pixels in a scene that can record up to 490 bands ranging from 400 to 2500 nm [1]. One of the important tasks in hyperspectral image (HSI) applications is target detection, where the presence or absence of an interested target object in a pixel of HSI is determined by comparing the target spectrum and the pixel spectrum. A target can be categorised into multi-pixel, full-pixel and subpixel target if its size is larger than, equal to or smaller than the ground sampling distance, respectively. Target detection is a challenging problem for two reasons. First, the spectra of objects are highly variable due to radiometric and atmospheric variations. Second, in the subpixel case, a pixel containing target will be mixed by the target object and the background (non-target) object, thus the collected spectrum is a combination of spectra of different materials. These two factors result in a dramatic difference between the target spectrum measured in the laboratory environment and that measured in real scenes.

Target detection methods can be classified as signature-based methods or sparse representation-based methods, depending on the availability of prior knowledge about target spectral characteristics [2]. Signature-based methods require the user to provide information of the target in the form of a single spectrum or a subspace and model the background by using probability distributions [3] or subspaces [4, 5]. For example, adaptive matched filter (AMF) [3] and constrained energy minimisation (CEM) [6] are classical approaches built on a single target spectrum; matched subspace detector (MSD) [5] and MSD with interaction effects (MSDinter) [7] built on a target subspace. Methods of this type are suitable for targets of any sizes, but their performances rely on the accuracy of prior target information. Sparse representation-based methods [8, 9] describe an observed spectrum as a sparse linear combination of training samples from the target class and the background class. These methods depend less on the accuracy of individual target spectrum, but they only work well when there are sufficient samples for each target.

While methods including iterative estimation [10] and multi-instance learning [11] have been proposed to improve a single target spectral signature, few work has been done on improving the target-background subspace used in MSD, a classical and widely-adopted

subspace-based method for subpixel target detection. Instead of simply concatenating the target subspace matrix and the background subspace matrix, in this paper we propose to learn a representative target-background mixed subspace directly from data. As spectral information of target is generally scarce and often only one library spectrum is available, we will first augment target data by synthesising target-background mixed spectra. Specifically, if the light ray is assumed to interact with ground materials only once before it reaches the sensor, we synthesise data based on linear mixing model (LMM); if we assume second-order interaction, then two classical bilinear mixing models (BMM) are adopted. Next, we learn the target-background mixed subspace by applying principal component analysis (PCA) to synthetic data. Performing the generalised likelihood ratio test, we obtain two new target detectors, called data-augmented MSD (DAMSD) in the case of linearly mixed data and data-augmented MSDinter (DAMSDI) in the case of bilinearly mixed data.

The main contributions of this paper are summarised as follows:

1. We propose two new approaches to HSI target detection called DAMSD and DAMSDI, which address the scarcity issue of target spectra and improve the target-background subspace estimation in MSD and MSDinter.
2. We provide two ways of synthesising target-background mixed spectra and prove the capability of the methods in representing any target spectrum in the scene with first-order or second-order scatterings.
3. We justify that the target-background mixed subspace constructed via PCA extracts the target information that is more discriminative from the background and improves both numerical stability and computational speed of the detector.

The rest of this paper is organised as follows. Section 2 reviews MSD and MSDinter. Section 3 introduces the data-augmentation method and proposes new target detectors. Section 4 presents experiment results on two public real hyperspectral image datasets. Section 5 concludes the paper and suggests future work.

2. Binary hypothesis testing model for HSI target detection

The task of target detection can be formulated as a statistical question of binary hypothesis testing and the decision is made based on the likelihood ratio test (LRT). Given an observed spectrum $\boldsymbol{x}$, the binary hypotheses are formed as follows:

$$\begin{aligned} H_0 &: \text{target absent in } \boldsymbol{x}; \\ H_1 &: \text{target present in } \boldsymbol{x}. \end{aligned} \tag{1}$$

Treating $\boldsymbol{x}$ as a random vector with a specific probability distribution $p(\boldsymbol{x})$, the LRT is given by

$$\mathrm{LR}(\boldsymbol{x}) = \frac{p(\boldsymbol{x}|H_1)}{p(\boldsymbol{x}|H_0)}. \tag{2}$$

If the detection statistic $\mathrm{LR}(\boldsymbol{x})$ exceeds a pre-defined threshold η, then H_1 is accepted as the most likely hypothesis and thus $\boldsymbol{x}$ will be labelled as target. If $\mathrm{LR}(\boldsymbol{x}) < \eta$, then $\boldsymbol{x}$ will be labelled as background.

In practice, the distribution of $\boldsymbol{x}$ includes some unknown parameters. Replacing these parameters by their maximum likelihood estimators (MLEs) in the LRT leads to the generalised likelihood ratio test (GLRT):

$$\mathrm{GLR}(\boldsymbol{x}) = \frac{\max_{\omega_1} p(\boldsymbol{x}|H_1)}{\max_{\omega_0} p(\boldsymbol{x}|H_0)} = \frac{p(\boldsymbol{x};\hat{\omega}_1)}{p(\boldsymbol{x};\hat{\omega}_0)} \underset{H_0}{\overset{H_1}{\gtrless}} \eta, \tag{3}$$

where ω_0 and ω_1 denote the unknown parameters in the probability distribution conditioned on H_0 and H_1, respectively; and $\hat{\omega}_0$ and $\hat{\omega}_1$ are the corresponding MLEs.

2.1. Matched subspace detector (MSD)

In the matched subspace detector (MSD), the spectrum vector is restricted to lie in a low-dimensional subspace of the spectral band space. As a linear mixing model, any spectrum from the pixel containing only background materials will be modelled as a linear combination of background bases, and any spectrum from the pixel containing the subpixel target material will be modelled as a linear combination of target and background bases. In other words, the binary hypotheses associated to the MSD are given as follows: for an L-dimensional hyperspectral spectrum $\boldsymbol{x}$,

$$\begin{aligned} H_0 &: \boldsymbol{x} = \boldsymbol{S}_b\boldsymbol{\alpha}_{b,0} + \boldsymbol{w}_b \qquad \text{(target absent)}; \\ H_1 &: \boldsymbol{x} = \boldsymbol{S}_t\boldsymbol{\alpha}_t + \boldsymbol{S}_b\boldsymbol{\alpha}_{b,1} + \boldsymbol{w}_t \qquad \text{(target present)}, \end{aligned} \tag{4}$$

where the matrices $\boldsymbol{S}_b \in \mathbb{R}^{L\times r_b}$ and $\boldsymbol{S}_t \in \mathbb{R}^{L\times r_t}$ represent the background subspace and the target subspace, respectively; $\boldsymbol{\alpha}_{b,0}$ and $\boldsymbol{\alpha}_{b,1}$ denote the coefficient vectors of $\boldsymbol{S}_b$, $\boldsymbol{\alpha}_t$ denotes the coefficient vector of $\boldsymbol{S}_t$; $\boldsymbol{w}_b$ and $\boldsymbol{w}_t$ are assumed to be Gaussian white noise vectors with variances σ_b^2 and σ_t^2, respectively: $\boldsymbol{w}_b \sim \mathcal{N}(\boldsymbol{0}, \sigma_b^2\boldsymbol{I})$ and $\boldsymbol{w}_t \sim \mathcal{N}(\boldsymbol{0}, \sigma_t^2\boldsymbol{I})$; and $\boldsymbol{I}$ denotes the identity matrix. The low dimensionality constraint on subspaces requires the number of columns in subspace matrices $\boldsymbol{S}_b$ and $\boldsymbol{S}_t$ to be smaller than the dimension of original data space, i.e. $r_b, r_t < L$. For the sake of notational simplicity, we introduce notations $\boldsymbol{S}_L = [\boldsymbol{S}_t,\ \boldsymbol{S}_b]$ and $\boldsymbol{\alpha}_L = [\boldsymbol{\alpha}_t,\ \boldsymbol{\alpha}_{b,1}]$ to denote the concatenation of subspace matrices and that of coefficient vectors, respectively.

The background subspace $\boldsymbol{S}_b$ is often unknown and thus should be estimated from background spectra in the HSI. In [12], principal component analysis (PCA) is used to identify component spectra. The leading eigenvectors of the background covariance matrix, which represent the linearly independent sources of spectral variation, are taken as columns of the background subspace. The target subspace may be specified by the user or constructed by using PCA if data are available.

The GLR for the hypotheses given in Eq. (4) is then written as

$$\mathrm{GLR}(\boldsymbol{x}) = \frac{\mathcal{L}(\hat{\boldsymbol{\alpha}}_L, \hat{\sigma}_t^2; \boldsymbol{x})}{\mathcal{L}(\hat{\boldsymbol{\alpha}}_b, \hat{\sigma}_b^2; \boldsymbol{x})} = \left[\frac{\boldsymbol{x}^T(\boldsymbol{I}-\boldsymbol{P}_b)\boldsymbol{x}}{\boldsymbol{x}^T(\boldsymbol{I}-\boldsymbol{P}_L)\boldsymbol{x}}\right]^{L/2}, \tag{5}$$

where $\mathcal{L}$ denotes the likelihood function with the MLEs $\hat{\boldsymbol{\alpha}}_L$, $\hat{\boldsymbol{\alpha}}_b$, $\hat{\sigma}_t^2$, $\hat{\sigma}_b^2$; $\boldsymbol{P}_b = \boldsymbol{S}_b(\boldsymbol{S}_b^T\boldsymbol{S}_b)^{-1}\boldsymbol{S}_b^T = \boldsymbol{S}_b\boldsymbol{S}_b^T$ is the projection matrix onto the column space of $\boldsymbol{S}_b$; and $\boldsymbol{P}_L = \boldsymbol{S}_L(\boldsymbol{S}_L^T\boldsymbol{S}_L)^{-1}\boldsymbol{S}_L^T$ is the projection matrix onto the column space of $\boldsymbol{S}_L$.

Applying a monotonic transformation on the GLR, the MSD is obtained as

$$D_{\mathrm{MSD}} = \mathrm{GLR}(\boldsymbol{x})^{2/L} - 1 = \frac{\boldsymbol{x}^T(\boldsymbol{P}_L-\boldsymbol{P}_b)\boldsymbol{x}}{\boldsymbol{x}^T(\boldsymbol{I}-\boldsymbol{P}_L)\boldsymbol{x}} \underset{H_0}{\overset{H_1}{\gtrless}} \eta. \tag{6}$$

However, concatenating $\boldsymbol{S}_t$ and $\boldsymbol{S}_b$ in H_1 may be ineffective for two reasons. First, learning the $\boldsymbol{S}_b$ that explains the largest amount of spectral variability of background spectra cannot guarantee that the spectral variability of target spectra is well explained. Second, a matrix inversion is required to compute $\boldsymbol{P}_L$, which has a computational complexity of $O(L^3)$. Meanwhile, if any column vector of $\boldsymbol{S}_t$ is nearly a linear combination of columns of

$\boldsymbol{S}_b$, then $\boldsymbol{S}_L$ will be ill-conditioned and result in large numerical errors when inverting the matrix [13].

2.2. Matched subspace detector with interaction effects (MSDinter)

The MSD is built on the assumption that any spectrum is a linear combination of subspace bases. In reality, however, as photons may interact with multiple objects before entering the sensor, the collected spectrum may be a non-linear combination of component spectra. Our previous work [7] extends the H_1 of MSD by modelling the second-order scatterings between target components and background components as an inter-crossing term, i.e.

$$\begin{aligned} H_0 &: \boldsymbol{x} = \boldsymbol{S}_b\boldsymbol{\alpha}_{b,0} + \boldsymbol{w}_b && \text{(target absent)}; \\ H_1 &: \boldsymbol{x} = \boldsymbol{S}_t\boldsymbol{\alpha}_t + \boldsymbol{S}_b\boldsymbol{\alpha}_{b,1} + \boldsymbol{S}_{\text{inter}}\boldsymbol{\alpha}_{\text{inter}} + \boldsymbol{w}_t && \text{(target present)}, \end{aligned} \tag{7}$$

where $\boldsymbol{S}_{\text{inter}} = [\boldsymbol{S}_{t,1}\odot\boldsymbol{S}_{b,1}, \cdots, \boldsymbol{S}_{t,1}\odot\boldsymbol{S}_{b,r_b}, \boldsymbol{S}_{t,2}\odot\boldsymbol{S}_{b,1}, \cdots, \boldsymbol{S}_{t,2}\odot\boldsymbol{S}_{b,r_b}, \cdots, \boldsymbol{S}_{t,r_t}\odot\boldsymbol{S}_{b,1}, \cdots, \boldsymbol{S}_{t,r_t}\odot\boldsymbol{S}_{b,r_b}]$ represents r_br_t pairs of interactions between bases in the target subspace ($\boldsymbol{S}_{t,i}$) and bases in the background subspace ($\boldsymbol{S}_{b,i}$); $\odot$ denotes the element-wise multiplication between two column vectors; and $\boldsymbol{\alpha}_{\text{inter}}$ denotes the coefficient vector associated with $\boldsymbol{S}_{\text{inter}}$. Again, we simplify the notation through concatenating matrices and vectors as $\boldsymbol{S}_I = [\boldsymbol{S}_t,\ \boldsymbol{S}_b,\ \boldsymbol{S}_{\text{inter}}]$ and $\boldsymbol{\alpha}_I = [\boldsymbol{\alpha}_t,\ \boldsymbol{\alpha}_{b,1},\ \boldsymbol{\alpha}_{\text{inter}}]$.

As with the MSD, the target detector called MSDinter is derived from the GLR and given by

$$D_{\text{MSDinter}} = \text{GLR}(\boldsymbol{x})^{2/L} = \frac{\boldsymbol{x}^T(\boldsymbol{I}-\boldsymbol{P}_b)\boldsymbol{x}}{\boldsymbol{x}^T(\boldsymbol{I}-\boldsymbol{P}_I)\boldsymbol{x}} \underset{H_0}{\overset{H_1}{\gtrless}} \eta, \tag{8}$$

where $\boldsymbol{P}_I = \boldsymbol{S}_I(\boldsymbol{S}_I^T\boldsymbol{S}_I)^{-1}\boldsymbol{S}_I^T$.

The problem of numerical instability is more severe in MSDinter due to the additional concatenation of $\boldsymbol{S}_{\text{inter}}$. Moreover, given $\boldsymbol{S}_I$ is a matrix of $L \times (r_b + r_t + r_br_t)$, $\boldsymbol{S}_I^T\boldsymbol{S}_I$ may even be non-invertible if $r_b > L/2$.

3. The data-augmented matched subspace detectors

Instead of simply concatenating the target subspace and the background subspace to represent the target-background subspace for the pixels mixing target and background, it

is desirable to learn a target-background mixed subspace directly from target-background mixed spectra by using PCA, for at least two benefits. Firstly, PCA can identify the components that explain the greatest amount of spectral variability of a target spectrum which is mixed by background in subpixel target detection problems, thus creating a more representative subspace for the mixed target. Secondly, as all column vectors of the new mixed subspace obtained by such data learning rather than matrix concatenating are now orthonormal, we can avoid the matrix inversion operation in Eqs. (6) and (8), leading to an improvement in numerical stability and computational speed.

Despite these benefits, it is hardly possible to learn an informative target-background mixed subspace in practice due to the scarcity of target spectra. To address this issue, we will propose two ways of synthesising target-background mixed spectra in this section – one describes the first-order scattering between spectra as in MSD, and the other describes the second-order scattering as in MSDinter. From these synthetic data, we construct a target-background mixed subspace with a set of orthonormal vectors, which will replace the concatenated subspace used in the alternative hypothesis H_1 of MSD and MSDinter, and the resultant new target detectors are called DAMSD and DAMSDI hereafter.

3.1. Data-augmented matched subspace detector (DAMSD)

Given N background spectra collected in the HSI, we synthesise the same number of target-background mixed spectra based on the linear mixing model (LMM) [14], i.e. a convex combination of the prior target spectrum and a background spectrum:

$$\boldsymbol{t}_{\mathrm{LMM},n} = \gamma_n \boldsymbol{t}_{\mathrm{prior}} + \zeta_n \boldsymbol{b}_n, \tag{9}$$

where $n \in \{1, \ldots, N\}$ is an index for the spectrum, $\boldsymbol{t}_{\mathrm{prior}}$ denotes the prior target spectrum commonly measured in a laboratory and $\boldsymbol{b}_n$ denotes the background spectrum of the nth pixel in the collected HSI; and γ_n is a random number sampled from a uniform distribution $U(0.05, 1)$. As the target pixels are sparse in the HSI, we treat the spectra of all pixels as background spectra; that is, N equals to the total number of pixels in the HSI. The proportion of the target material in a pixel is determined via γ_n. As its true value is unknown and varying across pixels, we choose γ_n randomly from the uniform distribution

to imply that values within the range are allowed and equally likely to exist in the synthetic data. The lower bound is set to be 0.05 to ensure that the target-background mixed spectra contain at least some spectral information of target. The upper bound is set to be 1 to allow for the existence of a pure target pixel. Following the sum-to-one constraint in LMM, we set $\zeta_n = 1 - \gamma_n$.

With abundant target information after such a data augmentation, it is now possible to learn a target-background mixed subspace using PCA. Accordingly, the binary hypotheses will be modified as

$$\begin{aligned} H_0 &: \boldsymbol{x} = \boldsymbol{S}_b \boldsymbol{\alpha}_b + \boldsymbol{w}_b \qquad \text{(target absent)}; \\ H_1 &: \boldsymbol{x} = \boldsymbol{S}_{tb} \boldsymbol{\alpha}_{tb} + \boldsymbol{w}_t \qquad \text{(target present)}, \end{aligned} \tag{10}$$

where $\boldsymbol{S}_{tb} \in \mathbb{R}^{L \times r_{tb}}$ represents the target-background mixed subspace constructed from PCA, and $\boldsymbol{\alpha}_{tb}$ is the coefficient vector of $\boldsymbol{S}_{tb}$.

Following the derivation of MSD, we apply the GLR test and obtain the following target detector, termed DAMSD:

$$D_{\text{DAMSD}} = \frac{\boldsymbol{x}^T (\boldsymbol{I} - \boldsymbol{P}_b) \boldsymbol{x}}{\boldsymbol{x}^T (\boldsymbol{I} - \boldsymbol{P}_{tb}) \boldsymbol{x}} \underset{H_0}{\overset{H_1}{\gtrless}} \eta, \tag{11}$$

where $\boldsymbol{P}_{tb} = \boldsymbol{S}_{tb} (\boldsymbol{S}_{tb}^T \boldsymbol{S}_{tb})^{-1} \boldsymbol{S}_{tb}^T = \boldsymbol{S}_{tb} \boldsymbol{S}_{tb}^T$. Note that the leading eigenvectors obtained from PCA are orthonormal and thus $(\boldsymbol{S}_{tb}^T \boldsymbol{S}_{tb})^{-1}$ is an identity matrix and $\boldsymbol{P}_{tb}$ is simplified as above.

The number of eigenvectors is a tuning parameter in constructing the optimal subspace. It also determines the number of coefficients that needs to be estimated. From the perspective of PCA, selecting a larger number of eigenvectors could explain more spectral variability. From the perspective of regression, given that the number of spectral bands is fixed, using more eigenvectors as predictors faces the risk of overfitting. In MSD, we only have to tune one parameter, namely the number of eigenvectors in the background subspace (r_b); the number of eigenvectors in the concatenated target-background subspace equals to r_b plus the number of prior target spectra supplied by the user (r_t). The DAMSD has two tuning parameters, namely r_b and r_{tb}, for the numbers of eigenvectors of the background subspace and the target-background mixed subspaces, respectively. To ensure that the DAMSD is a more parsimonious model than the MSD, we impose constraints on r_b and

r_{tb} as follows: $r_b^{\text{DAMSD}} \leq r_{b,\text{opt}}^{\text{MSD}}$ and $r_{tb}^{\text{DAMSD}} \leq r_{b,\text{opt}}^{\text{MSD}} + r_t$, where $r_{b,\text{opt}}^{\text{MSD}}$ denotes the optimal number of eigenvectors in the background subspace used in MSD that gives the best target detection performance. This condition guarantees that the DAMSD always uses fewer predictors than the MSD and thus fewer parameters need to be estimated. In the experiment section, we will evaluate the DAMSD with and without the constraints, to justify the value of these constraints.

Learning a target-background mixed subspace would be useful for subpixel target detection only if the synthetic data could represent mixed target spectra in the scene. We will now show that synthesising target-background mixed spectra using Eq. (9) is capable of recovering any target spectrum if the light ray interacts only once with the ground material.

Assumption 1. Let $\boldsymbol{e}_1^t, \ldots, \boldsymbol{e}_{m_t}^t$ denote the endmembers in an HSI that represent target materials, $\boldsymbol{e}_1^b, \ldots, \boldsymbol{e}_{m_b}^b$ denote the background endmembers, and $a_1^t, \ldots, a_{m_t}^t, a_1^b, \ldots, a_{m_b}^b$ denote the corresponding abundance coefficients. Let f denote a non-linear mixing function of endmembers for a background spectrum and g denote a non-linear mixing function of endmembers for a subpixel target spectrum. Assume that f and g have the following forms:

$$\begin{aligned} f(\boldsymbol{e}_1^b, \cdots, \boldsymbol{e}_{m_b}^b) &= \sum_{i=1}^{m_b} a_i^b \boldsymbol{e}_i^b + \Delta \\ g(\boldsymbol{e}_1^t, \cdots, \boldsymbol{e}_{m_t}^t, \boldsymbol{e}_1^b, \cdots, \boldsymbol{e}_m^b) &= \sum_{i=1}^{m_t} a_i^t \boldsymbol{e}_i^t + \sum_{i=1}^{m_b} a_i^b \boldsymbol{e}_i^b + \Delta, \end{aligned} \tag{12}$$

where Δ is a small constant.

The assumption in terms of Eq. (12) states that any interaction between spectra whose order is higher than one is negligible. It also constrains the form of non-linear mixing functions, from which we could prove the following proposition.

Proposition 1. Under Assumption 1, any real target spectrum $\boldsymbol{t}^{\text{real}}$ can be recovered from a set of synthetic spectra $\boldsymbol{t}_{\text{mix}}$ that are mixed with $K+1$ background spectra whose abundance vectors are linearly independent and by using Eq. (9), where K denotes the number of pure background endmembers in an HSI.

Proof. Under Assumption 1, any real target spectrum, denoted by $\boldsymbol{t}^{\text{real}}$, can be represented by using a function g as

$$\boldsymbol{t}^{\text{real}} = g(\boldsymbol{t}, \boldsymbol{b}_1, \cdots, \boldsymbol{b}_K) = \alpha\boldsymbol{t} + \sum_{i=1}^{K} \beta_i \boldsymbol{b}_i + \Delta, \tag{13}$$

where $\boldsymbol{t}$ denotes the prior target spectrum; $\boldsymbol{b}_1, \ldots, \boldsymbol{b}_K$ denote K background endmembers, each of which represents a pure background object, and they are typically unknown yet deterministic. The abundance vector of each observed target spectrum, denoted by $(\alpha, \beta_1, \ldots, \beta_K)$, is also unknown and deterministic. There are $1 + K$ coefficients in total.

Under Assumption 1, any real background spectrum observed at the nth pixel, denoted as $\boldsymbol{b}_n^{\text{real}}$, can be represented using a function f as

$$\boldsymbol{b}_n^{\text{real}} = f_n(\boldsymbol{b}_1, \cdots, \boldsymbol{b}_K) = \sum_{i=1}^{K} \beta_{n,i} \boldsymbol{b}_i + \Delta. \tag{14}$$

f_n follows the assumption specified in Eq. (12) and the subscript n is used to remind that the abundance vector $(\beta_1, \ldots, \beta_K)$ is different for different real background spectra.

Following the mixing strategy in Eq. (9), a synthetic target-background mixed spectrum is given by

$$\boldsymbol{t}_{\text{mix},n} = \gamma_n \boldsymbol{t} + (1 - \gamma_n)\boldsymbol{b}_n^{\text{real}} = \gamma_n \boldsymbol{t} + \sum_{i=1}^{K} (1 - \gamma_n)\beta_{n,i} \boldsymbol{b}_i + \Delta. \tag{15}$$

Eqs. (13) and (15) have exactly the same functional form but differ in their coefficients of $(\boldsymbol{t}, \boldsymbol{b}_1, \ldots, \boldsymbol{b}_K)$. Synthesising N target-background mixed spectra and recording their coefficients, i.e. $(\gamma_n, (1 - \gamma_n)\beta_{n,1}, \ldots, (1 - \gamma_n)\beta_{n,K})$, generate a coefficient matrix of size $(1 + K) \times N$. If this coefficient matrix has full row rank, then we can represent the coefficient vector in Eq. (13) as a linear combination of column vectors of the coefficient matrix. In other words, we can recover $\boldsymbol{t}^{\text{real}}$ by representing its unique coefficient vector of $(\boldsymbol{t}, \boldsymbol{b}_1, \ldots, \boldsymbol{b}_K)$ based on $(K + 1)$ linearly independent coefficient vectors. □

On the one hand, as each background endmember corresponds to a distinct background material and there are only a limited number of materials in an HSI, K is a relatively small number. On the other hand, as an HSI collects data over a large spatial area, the number of pixels N is generally large. Mixing each background spectrum with the library

target spectrum will synthesise N target-background mixed spectra. It is reasonable to speculate that, out of N synthesised spectra, there exists a set of $(K+1)$ spectra whose abundance vectors are linearly independent and thus any real target spectrum with first-order scatterings can be represented and recovered as a linear combination of these spectra.

3.2. Data-augmented matched subspace detector with interaction effects (DAMSDI)

To characterise the multiple scattering effect, we adopt two classical hyperspectral non-linear mixing models, both of which add bilinear interaction terms to the LMM, i.e.

$$\boldsymbol{x} = a_i \boldsymbol{e}_i + a_j \boldsymbol{e}_j + a_{ij} \boldsymbol{e}_i \odot \boldsymbol{e}_j + \boldsymbol{w}, \tag{16}$$

where $\boldsymbol{e}_i$ and $\boldsymbol{e}_j$ denote endmembers; a_i, a_j, a_{ij} denote the abundance coefficients and represent the fraction of pixel area covered by the corresponding materials. In Singer and McCord's model [15], the interaction term is regarded as an artificial third endmember. Thus, the abundance vector is constrained to sum to one to express that the observed spectrum can be fully described by the endmembers. In Fan's model [16], Eq. (16) is derived through approximating the non-linear mixing model by the second-order Taylor series and, as a result, $a_{ij} = a_i a_j$. This interaction coefficient has a clear physical interpretation that the probability of a light ray interacting with two endmembers depends on the areal fraction of each endmember [17]. These bilinear mixing models (BMMs) are applied to interaction phenomena caused by two layers of materials, such as a layer of vegetation above the soil, or a secondary source of illumination reflected from another object [18].

Taking the above two physical intuitions into account, we propose to synthesise target-background bilinearly mixed spectra as follows:

$$\boldsymbol{t}_{\mathrm{BMM},n} = \gamma_n \boldsymbol{t}_{\mathrm{prior}} + \zeta_n \boldsymbol{b}_n + \gamma_n \zeta_n \boldsymbol{t}_{\mathrm{prior}} \odot \boldsymbol{b}_n, \tag{17}$$

where $\boldsymbol{t}_{\mathrm{prior}} \odot \boldsymbol{b}_n = \begin{pmatrix} t_{\mathrm{prior},1} b_{n,1} \\ t_{\mathrm{prior},2} b_{n,2} \\ \vdots \\ t_{\mathrm{prior,L}} b_{n,L} \end{pmatrix}$; γ_n is again a random number sampled from $U(0.05, 1)$. The coefficient of the interaction term is assumed to be $\gamma_n \zeta_n$ following [16] and $\gamma_n + \zeta_n +$

$\gamma_n\zeta_n = 1$ following [15]. From these two conditions, we derive ζ_n to be $\frac{1-\gamma_n}{1+\gamma_n}$. Note that Eq. (17) is different from Eq. (7) as we are now mixing the prior target spectrum with background spectra collected in the HSI, rather than mixing it with bases in the background subspace.

To detect the target, we apply the procedure used in DAMSD, that is, constructing a target-background mixed subspace $\boldsymbol{S}_{tb}$ by applying PCA to the synthetic data from Eq. (17), creating binary hypotheses as Eq. (10) and applying the GLR test. The target detector, termed DAMSDI, will have the same formula as Eq. (11); the projection matrix $\boldsymbol{P}_{tb} = \boldsymbol{S}_{tb}\boldsymbol{S}_{tb}^T$ in the equation will be different as $\boldsymbol{S}_{tb}$ is now different.

As we will show in Proposition 2, owing to the bilinear interaction terms, the data synthesised based on Eq. (17) could recover any real target spectrum with second-order scatterings. We start by modifying Assumption 1 to a slightly more general mixing functions.

Assumption 2. Let $\boldsymbol{e}_1^t, \ldots, \boldsymbol{e}_{m_t}^t$ denote the target endmembers, $\boldsymbol{e}_1^b, \ldots, \boldsymbol{e}_{m_b}^b$ denote the background endmembers, and $a_1^t, \ldots, a_{m_t}^t, a_1^b, \ldots, a_{m_b}^b$ denote the corresponding abundance coefficients. Assume the non-linear mixing functions f and g, representing a background spectrum and a subpixel target spectrum respectively, have the following forms:

$$\begin{aligned} f(\boldsymbol{e}_1^b, \cdots, \boldsymbol{e}_m^b) &= \sum_{i=1}^{m_b} a_i^b \boldsymbol{e}_i^b + \sum_{i=1}^{m_b}\sum_{j\geq i}^{m_b} a_i^b a_j^b \boldsymbol{e}_i^b \odot \boldsymbol{e}_j^b + \Delta \\ g(\boldsymbol{e}_1, \cdots, \boldsymbol{e}_m) &= \sum_{i=1}^{m_t+m_b} a_i \boldsymbol{e}_i + \sum_{i=1}^{m_t+m_b}\sum_{j\geq i}^{m_t+m_b} a_i a_j \boldsymbol{e}_i \odot \boldsymbol{e}_j + \Delta, \end{aligned} \tag{18}$$

where we simplify the notation by combining target and background endmembers as $(\boldsymbol{e}_1, \ldots, \boldsymbol{e}_{m_t+m_b}) = (\boldsymbol{e}_1^t, \ldots, \boldsymbol{e}_{m_t}^t, \boldsymbol{e}_1^b, \ldots, \boldsymbol{e}_{m_b}^b)$ and abundance coefficients as $(a_1, \ldots, a_{m_t+m_b}) = (a_1^t, \ldots, a_{m_t}^t, a_1^b, \ldots, a_{m_b}^b)$; Δ is a small constant.

Eq. (18) states that any interaction whose order is higher than two is negligible.

Proposition 2. Under Assumption 2, any real target spectrum $\boldsymbol{t}^{\text{real}}$ can be recovered from a set of synthetic spectra $\boldsymbol{t}_{\text{mix}}$ that are mixed with $(K+1)^2$ background spectra whose abundance vectors are linearly independent and by using Eq. (17), where K denotes the number of pure background endmembers in an HSI.

Proof. Under Assumption 2, any real target-background spectrum $\boldsymbol{t}^{\text{real}}$ has the following expression

$$\boldsymbol{t}^{\text{real}} = g(\boldsymbol{t}, \boldsymbol{b}_1, \cdots, \boldsymbol{b}_K) = \alpha\boldsymbol{t} + \sum_{i=1}^{K} \beta_i \boldsymbol{b}_i + \sum_{i=1}^{K} \alpha\beta_i \boldsymbol{t} \odot \boldsymbol{b}_i + \sum_{i=1}^{K}\sum_{j\geq i}^{K} \beta_i\beta_j \boldsymbol{b}_i \odot \boldsymbol{b}_j + \Delta. \quad (19)$$

The number of coefficients equals to $(1 + K + K + K(K+1)/2) = \frac{1}{2}K^2 + \frac{5}{2}K + 1$.

Under the same assumption, any real background spectrum $\boldsymbol{b}_n^{\text{real}}$ has the expression

$$\boldsymbol{b}_n^{\text{real}} = f_n(\boldsymbol{b}_1, \cdots, \boldsymbol{b}_K) = \sum_{i=1}^{K} \beta_{n,i} \boldsymbol{b}_i + \sum_{i=1}^{K}\sum_{j\geq i}^{K} \beta_{n,i}\beta_{n,j} \boldsymbol{b}_i \odot \boldsymbol{b}_j + \Delta. \quad (20)$$

A target-background mixed spectrum synthesised from Eq. (17) with $\zeta_n = \frac{1-\gamma_n}{1+\gamma_n}$ is given by

$$\begin{aligned} \boldsymbol{t}_{\text{mix},n} &= \gamma_n \boldsymbol{t} + \zeta_n \boldsymbol{b}_n^{\text{real}} + \gamma_n\zeta_n \boldsymbol{t} \odot \boldsymbol{b}_n^{\text{real}} \\ &= \gamma_n \boldsymbol{t} + \sum_{i=1}^{K} \zeta_n\beta_{n,i} \boldsymbol{b}_i + \sum_{i=1}^{K}\sum_{j\geq i}^{K} \zeta_n\beta_{n,i}\beta_{n,j} \boldsymbol{b}_i \odot \boldsymbol{b}_j + \sum_{i=1}^{K} \gamma_n\zeta_n\beta_{n,i} \boldsymbol{t} \odot \boldsymbol{b}_i + \Delta. \end{aligned} \quad (21)$$

From Eq. (21), we can obtain a coefficient matrix of size $(\frac{1}{2}K^2 + \frac{5}{2}K + 1) \times N$. If this coefficient matrix has full rank, some linear combination of its column vectors will equal to the coefficient vector of Eq. (19) and hence could represent $\boldsymbol{t}^{\text{real}}$. For $K > 1$, $\frac{1}{2}K^2 + \frac{5}{2}K + 1 < (K+1)^2$. Therefore, if we can find $(K+1)^2$ background spectra whose abundance vectors are linearly independent, then the full-rank condition on the coefficient matrix is guaranteed and $\boldsymbol{t}^{\text{real}}$ can be recovered. □

4. Experiments

In this section, we evaluate the effectiveness of DAMSD and DAMSDI on two public real hyperspectral image datasets, namely HyMap and MUUFL. In both datasets, the target has a size smaller than the ground sampling, suggesting the use of MSD for subpixel target detection. Moreover, the datasets provide only one library spectrum that can be used as the prior information on target, suggesting the need and potential of data augmentation. The HyMap dataset is a benchmark dataset for hyperspectral subpixel target detection [19, 20, 21, 22]. The MUUFL dataset provides two HSIs over the same scene, thus serving the

purpose of model validation [23, 24]. The proposed methods are compared against MSD, MSDinter and four classical target detection methods, namely CEM [6], AMF [3], signed ACE (sACE) [25] and OSP [4].

4.1. The HyMap dataset

4.1.1. Data description

Fig. 1a shows the HSI over Cooke City, MT, USA. It was collected by Rochester Institute of Technology in July 2006 using the HyMap sensor [26]. The image contains 126 spectral bands corresponding to wavelengths from 450 to 2500 nm with a 15 nm average spectral bandwidth and 280×800 pixels with approximately 3 meters of ground resolution.

In the HyMap dataset, four types of fabric panels (F1, F2, F3, F4) and three types of vehicles (V1, V2, V3) are prepared as targets. Fig. 1b shows their ground-truth locations and Table 1 lists information on target type, size, number of pixels used to define the region of interest (ROI), and number of pixels for the guard region; ROI is a region including a target; the guard region should not include any target pixels and is used to prevent the influence of target spectrum on background estimation. F3 and F4 have two samples with different sizes; F3a and F4a denote the sample with a size of 2m $\times$ 2m, and F3b and F4b denote the 1m $\times$ 1m sample.

Table 1: Target information in the HyMap dataset. 'n(ROI)' and 'n(Guard)' denote the number of pixels used to mark the target region and the guard region, respectively.

Target	Description	n(ROI)	n(Guard)
F1	red cotton, 3m $\times$ 3m	9	16
F2	yellow nylon, 3m $\times$ 3m	9	16
F3a	blue cotton, 2m $\times$ 2m	9	16
F3b	blue cotton, 1m $\times$ 1m	1	8
F4a	red nylon, 2m $\times$ 2m	9	16
F4b	red nylon, 1m $\times$ 1m	1	8
V1	Chevy Blazer	1	8
V2	Toyota T100	1	8
V3	Sabura GL Wagon	1	8

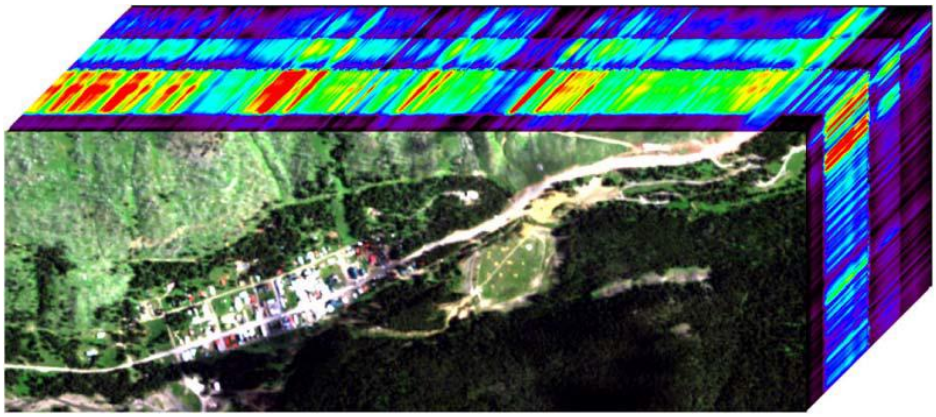

(a)

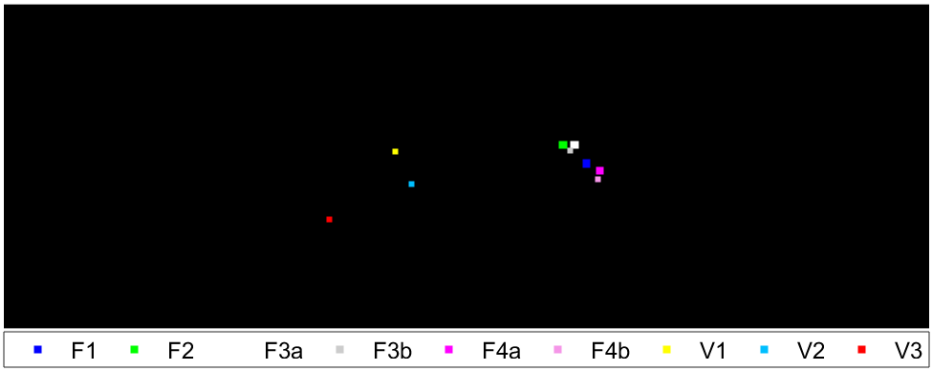

(b)

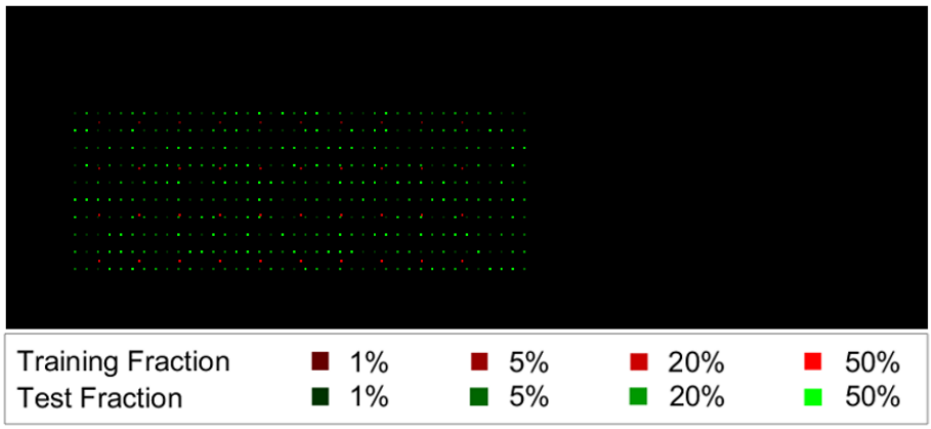

(c)

Figure 1: (a) The Hymap dataset with a size of $280 \times 800 \times 126$; (b) ground-truth locations of seven targets are marked in different colors; targets F3 and F4 come in two sizes and are marked separately as F3a, F3b, F4a and F4b, respectively; and background pixels are in black; (c) position and fraction of implanted targets in the training and test stages.

Fig. 2a shows the target spectra measured in the laboratory environment and Fig. 2b shows the spectra measured by the airborne sensor. We can clearly see a mismatch between two sets of spectra, which may be caused by imperfect radiometric and atmospheric correction and the mixing phenomenon between target and background objects. The latter issue has been particularly modelled in the alternative hypothesis of MSD-type methods.

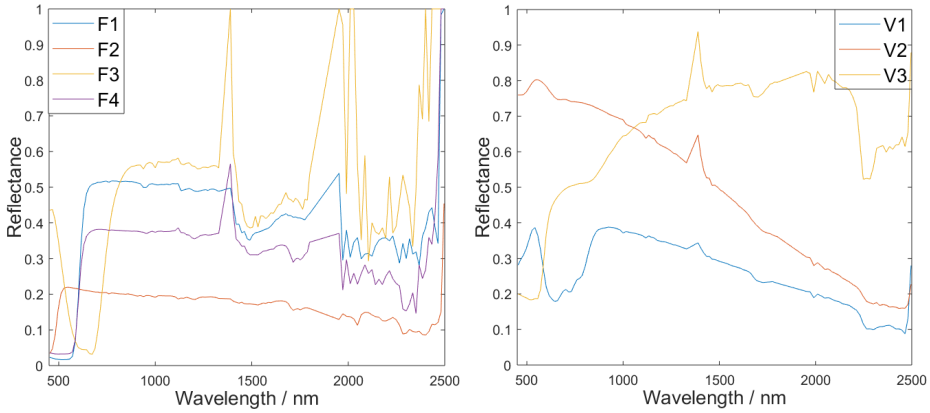

(a) measured in the laboratory environment

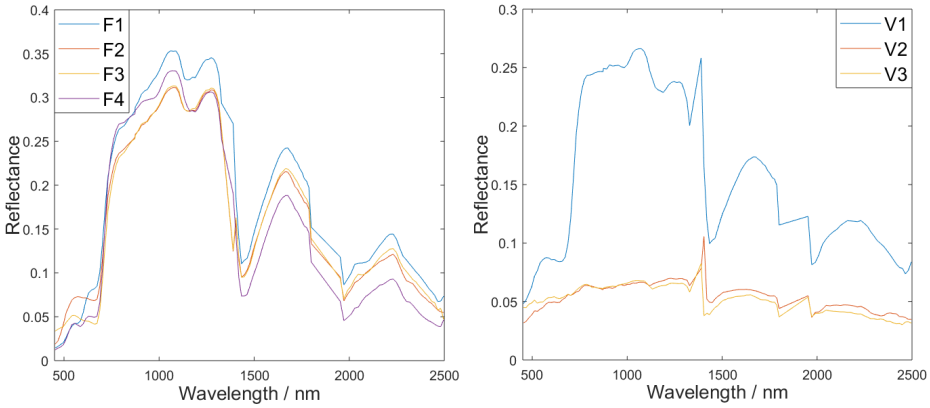

(b) measured by the airborne sensor

Figure 2: Reflectance spectra of seven targets in the HyMap dataset.

315

4.1.2. Experimental settings

Since there is only one sample for each target, we adopt the false alarm rate (FAR) as the evaluation criterion for the HyMap dataset. All the methods in our experiments identify a pixel as target if its detection statistic is larger than a pre-defined threshold.

Table 2: Parameters r_b, r_{tb} in subspace-based methods for the HyMap dataset.

	r_b					r_{tb}	
	OSP	MSD	MSDinter	DAMSD	DAMSDI	DAMSD	DAMSDI
F1	71	27	58	25	10	25	11
F2	38	21	37	21	14	19	11
F3a	25	11	32	6	5	11	6
F3b	111	111	29	11	5	11	6
F4a	67	51	56	41	51	35	39
F4b	53	53	117	53	3	52	2
V1	43	43	10	10	10	9	9
V2	4	2	21	2	2	3	3
V3	45	45	104	16	16	19	19

The threshold, however, is unknown and thus we set it as the largest detection statistic of pixels in the ROI. Any pixel outside of the ROI and guard region whose detection statistic is larger than this threshold is called a false alarm and the FAR is defined as the number of false alarms divided by the number of background pixels in the image; the number of background pixels equals to the total number of pixels in the image minus the number of pixels in the ROI and guard region. A target detection method is more effective if it has a lower FAR.

Targets will be detected in a sequential manner. That is, when one target is being detected, the other targets will be treated as the background. Moreover, pixels located in the guard region do not count as target nor background [27].

OSP, MSD, and MSDinter require the estimation of background subspace. Here we apply PCA to mean-centered pixels and select the first r_b principal components to form $\boldsymbol{S}_b$. MSD and MSDinter also require the estimation of target subspace. Since there is only one target spectrum, we subtract the background mean spectrum and normalise the centered spectrum to unit length with respect to L_2. In DAMSD and DAMSDI, the background subspace and the target-background mixed subspace are estimated based on background spectra and target-background mixed spectra, respectively. For these two methods, we do

Table 3: Target detection false alarm rates (FARs) for the HyMap dataset. Best results are in boldface.

	CEM	AMF	sACE	OSP	MSD	MSDinter	DAMSD	DAMSDI
F1	4.91e-05	4.91e-05	**0**	**0**	**0**	4.46e-06	4.46e-06	5.80e-05
F2	**0**	**0**	**0**	**0**	**0**	**0**	**0**	**0**
F3a	4.00e-02	4.14e-02	7.10e-02	1.67e-03	7.88e-03	**3.39e-04**	6.25e-04	1.67e-03
F3b	6.07e-02	8.89e-02	7.51e-02	1.29e-03	2.41e-03	4.69e-03	**8.57e-04**	1.70e-03
F4a	1.07e-04	1.07e-04	**0**	**0**	**0**	1.29e-04	4.46e-06	**0**
F4b	1.09e-02	2.21e-02	4.71e-02	7.86e-04	9.06e-04	1.59e-02	5.05e-03	**2.68e-04**
V1	1.88e-02	3.44e-02	1.51e-02	5.97e-03	1.33e-03	1.04e-02	**3.30e-04**	6.03e-04
V2	2.88e-01	5.06e-01	2.81e-01	1.23e-02	9.68e-03	2.29e-02	**5.96e-03**	7.26e-03
V3	1.19e-02	1.81e-02	7.33e-03	5.04e-03	3.31e-03	1.81e-02	4.64e-04	**4.33e-04**
sum	4.31e-01	7.11e-01	4.97e-01	2.71e-02	2.55e-02	7.25e-02	1.33e-02	**1.20e-02**

not mean center the spectra and apply PCA directly to the original background spectra and target-background mixed spectra. The reason is that the two sets of spectra have different mean values and, as the label of the test pixel is unknown, it is unclear about which mean value should be subtracted from it. As explained in Section 3.1, to obtain a more parsimonious model, the tuning parameters r_b, r_{tb} are searched under the constraints that $r_b^{\text{DAMSD}}, r_b^{\text{DAMSDI}} \leq r_{b,\text{opt}}^{\text{MSD}}$ and $r_{tb}^{\text{DAMSD}}, r_{tb}^{\text{DAMSDI}} \leq r_{b,\text{opt}}^{\text{MSD}} + 1$. Table 2 lists the optimal values of r_b, r_{tb} of OSP, MSD, MSDinter, DAMSD, and DAMSDI for each target.

4.1.3. Results and discussions

The detection results for all methods are listed in Table 3. Out of nine targets, DAMSD reduces the FARs of MSD on five targets and is as good as MSD on one target; DAMSDI outperforms MSDinter on six targets and performs equally well on one target. Compared with all methods excluding DAMSDI, DAMSD achieves the best performance on five targets; DAMSDI is optimal on six targets. The sum of FARs of DAMSD and DAMSDI are also smaller than other methods. This suggests the effectiveness of learning a target-background mixed subspace from synthetic data.

In addition to detection accuracy, the efficacy of target detectors could also be reflected in the separability between pixels that contain the target material and pixels that contain

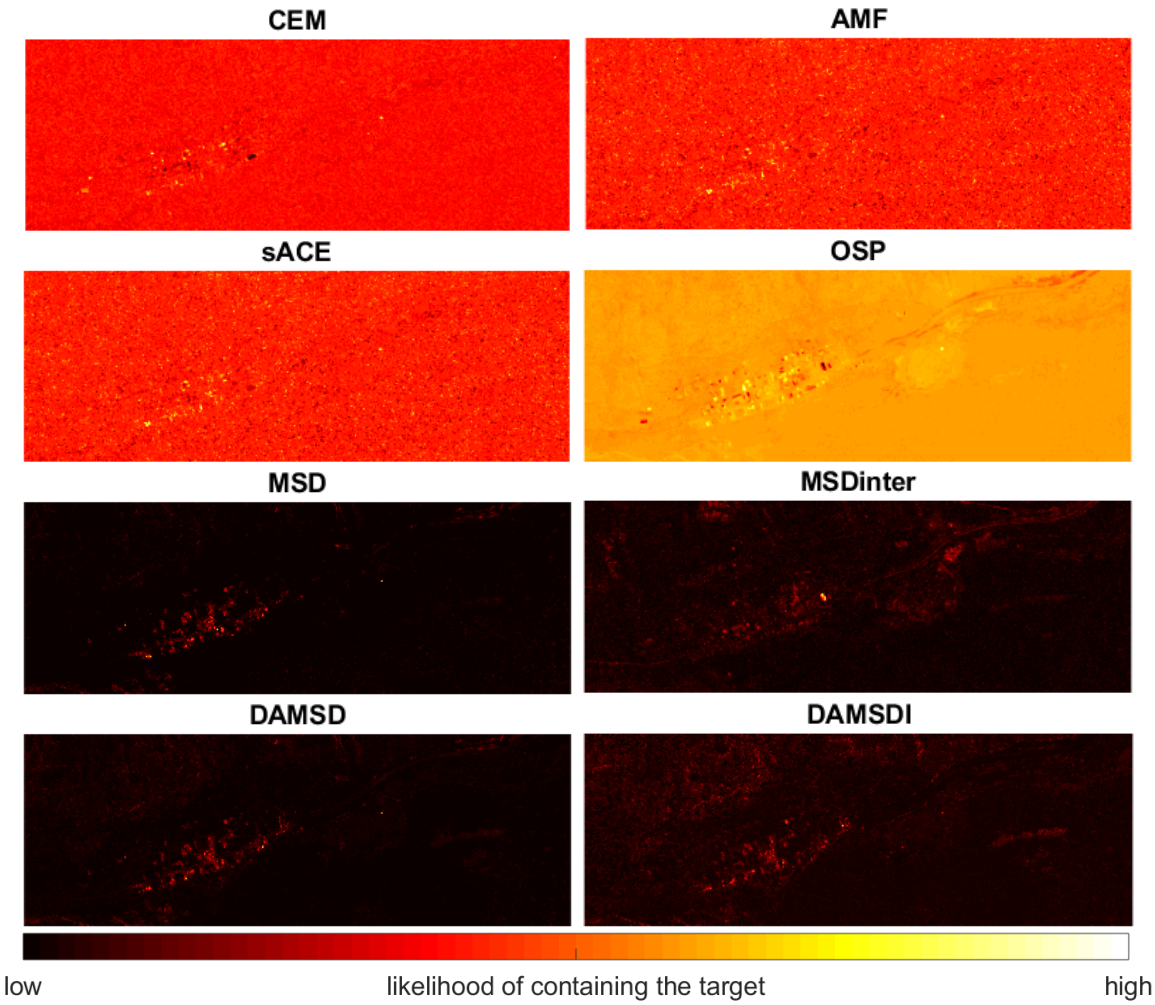

Figure 3: 2D plot of the detection statistics for target V2 in the HyMap dataset.

only background materials. In Fig. 3, we plot the detection statistic of all comparison methods for the subpixel target V2. We first notice that MSD and MSDinter distinguish target pixels from background pixels more clearly than other existing methods as very few background pixels have high detection statistics. The detection maps of DAMSD and DAMSDI are almost identical to the corresponding baselines, suggesting that the proposed methods maintain this advantage. Moreover, LMM-based methods are more effective in suppressing the background pixels than BMM-based ones.

Finally, we verify that the proposed methods could learn a more representative target-background mixed subspace. Fig. 4 shows the spectrum from the pixel containing target

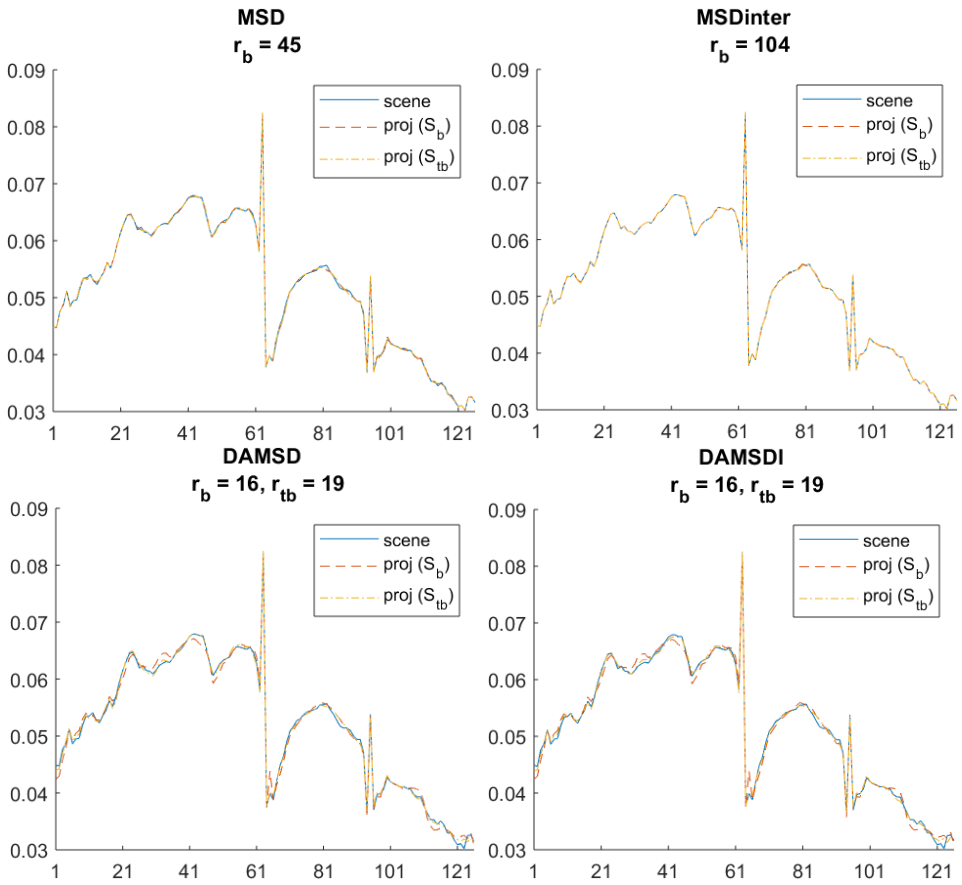

Figure 4: Projections of the spectrum of the pixel containing target V3 onto the background subspace S_b and target-background mixed subspace S_{tb}. The number of eigenvectors used to estimate S_b and S_{tb} are given by r_b, r_{tb}, respectively.

V3 and its projections onto the estimated background subspace, i.e. $\boldsymbol{P}_b\boldsymbol{x}$, and the target-background subspace, i.e. $\boldsymbol{P}_L\boldsymbol{x}$ (for MSD), $\boldsymbol{P}_I\boldsymbol{x}$ (for MSDinter) or $\boldsymbol{P}_{tb}\boldsymbol{x}$ (for DAMSD(I)), that give the lowest FAR. The subspaces estimated by MSD and MSDinter are built upon a large number of eigenvectors and thus almost fully represent the target spectrum. DAMSD and DAMSDI build more compact subspaces and thus the projections deviate more from the target spectrum. However, the subspaces estimated by DA-type methods are more discriminative as the projection onto the target-background mixed subspace lies closer to the target spectrum than the projection onto the background subspace. This clear distinction contributes to improved detection performance.

4.1.4. Simulation study

In this section, we manually implant multiple samples of targets F1–V3 into the image in order to create a training set and a test set on which MSD, MSDinter, DAMSD and DAMSDI will be evaluated. Moreover, we will examine the choices of parameters, including the target proportion in synthesising target-background mixed spectra and the number of eigenvectors in forming background subspace and target-background mixed subspace.

We generate 40 target-implanted spectra $\boldsymbol{x}$ in the training stage and 400 spectra in the test stage by using the library spectrum as the target spectrum $\boldsymbol{t}$, mixing the target spectrum linearly and bilinearly with the collected background spectrum $\boldsymbol{b}$ via the following two models, and adding additive zero-mean white Gaussian noise $\boldsymbol{n}$ [28, 29]:

- linearly implanted target:

$$\boldsymbol{x} = f_t\boldsymbol{t} + (1 - f_t)\boldsymbol{b} + \boldsymbol{n}; \tag{22}$$

- bilinearly implanted target:

$$\boldsymbol{x} = f_t\boldsymbol{t} + (1 - f_t - f_m)\boldsymbol{b} + f_m\boldsymbol{t} \odot \boldsymbol{b} + \boldsymbol{n}. \tag{23}$$

In the linear case, the implanted fraction f_t is set as $1\%, 5\%, 20\%, 50\%$; in the bilinear case, f_t is set as 1% and f_m is set as $1\%, 5\%, 20\%, 50\%$. The variance of the Gaussian noise at each band is set to match the signal-to-noise ratio of 30dB. The locations and fractions of implanted targets are shown in Fig. 1c. Pixels in the ROI and guard region of the target are replaced by randomly sampled background pixels. For all comparison methods, the background subspace and the target-background mixed subspace are constructed from the training data and used to detect targets in both training and test stages. The area under the receiver operating characteristic (ROC) curve (AUC) statistic is used to evaluate the detection performance, which will be carefully explained in Section 4.2.2.

Table 4 lists the training and test AUCs of MSD, MSDinter, DAMSD and DAMSDI. For linearly implanted targets, the proposed methods achieve similar average AUC to MSD in the training stage and higher average AUC of 0.02 in the test stage. For bilinearly implanted targets, the advantage is more distinct as the average AUC improves by 0.07 in

Table 4: Training and test AUCs on detecting linearly and bilinearly implanted targets. Boldface indicates the best performance; underline indicates the better one between DAMSD and DAMSDI.

Linearly implanted targets

	training AUCs				test AUCs			
	MSD	MSDinter	DAMSD	DAMSDI	MSD	MSDinter	DAMSD	DAMSDI
F1	0.9415	**0.9776**	0.9367	0.9272	0.9486	0.9281	**0.9537**	0.9290
F2	0.8504	**0.9682**	0.8563	0.8599	0.8256	**0.9488**	0.8292	0.8421
F3	0.9672	0.9666	0.9554	**0.9682**	**0.9793**	0.9349	0.9451	0.9750
F4	0.9412	0.9256	**0.9420**	0.9294	0.9461	0.3378	0.9531	**0.9750**
V1	0.9182	**0.9738**	0.9087	0.9166	0.8948	0.2896	0.9003	**0.9173**
V2	0.8926	0.9218	**0.9229**	0.9092	0.8763	0.2806	**0.9350**	0.9229
V3	0.9532	0.9532	0.9541	**0.9696**	0.8763	0.4328	0.9721	**0.9750**
average	0.9235	**0.9553**	0.9251	0.9257	0.9067	0.5932	0.9269	**0.9338**

Bilinearly implanted targets

	training AUCs				test AUCs			
	MSD	MSDinter	DAMSD	DAMSDI	MSD	MSDinter	DAMSD	DAMSDI
F1	0.9254	**0.9677**	0.9342	0.9462	0.9167	0.3565	0.9536	**0.9586**
F2	0.5461	**0.9941**	0.7099	0.7052	0.5071	**0.9657**	0.6791	0.6769
F3	**0.9982**	0.9359	0.9968	0.9938	**0.9969**	0.1636	0.9880	0.9945
F4	0.9331	0.9901	0.9380	**0.9491**	0.9240	0.9269	0.9555	**0.9599**
V1	0.8230	0.9890	0.9997	**0.9999**	0.8125	0.1246	**0.9981**	0.9976
V2	0.7265	**0.9651**	0.7918	0.7381	0.7604	0.7443	**0.7887**	0.7212
V3	0.8552	**0.9952**	0.9071	0.9384	0.8220	0.7734	0.8656	**0.9518**
average	0.8296	**0.9767**	0.8968	0.8958	0.8199	0.5793	0.8898	**0.8944**

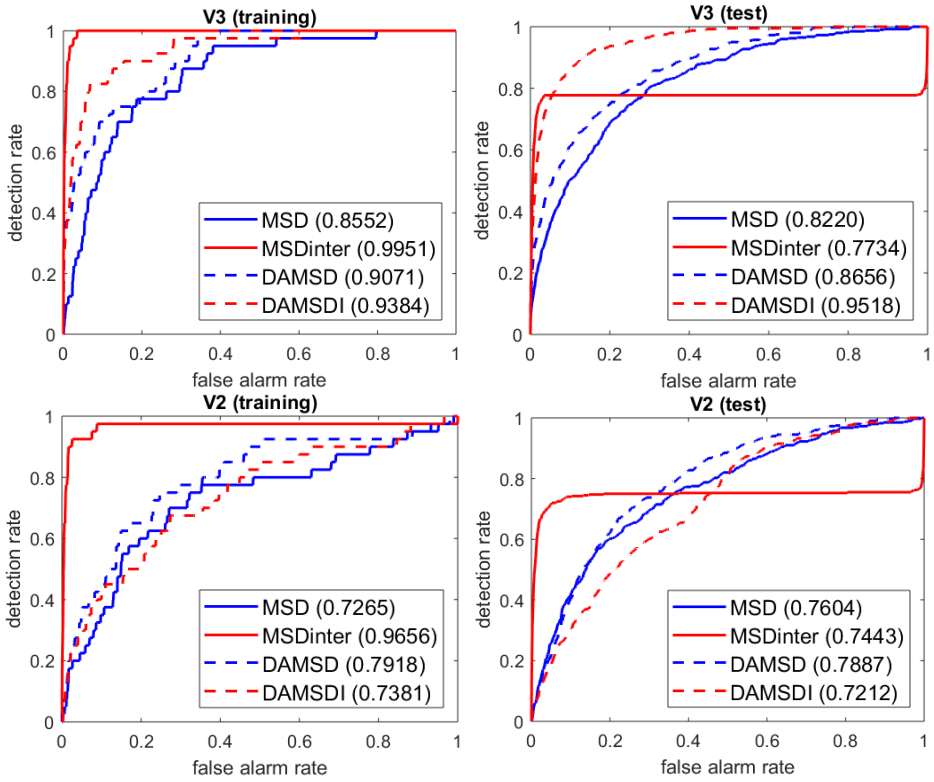

Figure 5: Training and test ROC curves for bilinearly implanted targets V3 and V2.

both training and test stages. MSDinter shows outstanding performance on the training data but deteriorates sharply on the test data, signifying overfitting; this issue does not arise in the proposed methods. DAMSDI is slightly superior to DAMSD for both linearly and bilinearly implanted targets as the majority of targets have higher AUCs and the average test AUC is also higher. In addition, we provide the training and test ROC curves for bilinearly implanted targets V3 and V2 in Fig. 5; V3 corresponds to the case where the proposed methods outperform MSD by a large margin and V2 corresponds to the case where the performance is less satisfactory. When DA-type methods have similar AUCs to MSD, e.g. in the training stage of V2, they also exhibit similar patterns of ROC curves.

The synthesis of target-background mixed spectra depends on γ_n, which represents the proportion of the target object in a pixel and is randomly sampled from a uniform distribution with a lower bound l of 0.05 and an upper bound u of 1. To better understand its influence on the detection performance, we select three values for u, namely 0.2, 0.5

Table 5: Effect of the target proportion γ_n on the training and test AUCs of DAMSDI for the bilinearly implanted targets. γ_n is randomly sampled from $U(0.05, u)$ and three values of u are compared. Median AUCs (in normal font size) and range of AUCs (in small font size) are reported with the best ones in bold.

	training AUCs			test AUCs		
	u=0.2	u=0.5	u=1	u=0.2	u=0.5	u=1
F1	$0.9442_{0.0000}$	$0.9414_{0.0001}$	$\mathbf{0.9462}_{0.0002}$	$0.9226_{0.0000}$	$0.9568_{0.0001}$	$\mathbf{0.9586}_{0.0001}$
F2	$\mathbf{0.7336}_{0.0002}$	$0.7237_{0.0001}$	$0.7052_{0.0000}$	$0.6420_{0.0002}$	$\mathbf{0.6851}_{0.0000}$	$0.6769_{0.0000}$
F3	$0.9944_{0.0001}$	$\mathbf{0.9947}_{0.0001}$	$0.9938_{0.0001}$	$0.9911_{0.0001}$	$0.9920_{0.0001}$	$\mathbf{0.9945}_{0.0000}$
F4	$0.9467_{0.0000}$	$0.9445_{0.0001}$	$\mathbf{0.9491}_{0.0002}$	$0.9278_{0.0000}$	$0.9584_{0.0001}$	$\mathbf{0.9598}_{0.0001}$
V1	$\mathbf{0.9999}_{0.0000}$	$\mathbf{0.9999}_{0.0000}$	$\mathbf{0.9999}_{0.0000}$	$\mathbf{0.9989}_{0.0000}$	$0.9976_{0.0000}$	$0.9976_{0.0000}$
V2	$0.7398_{0.0004}$	$\mathbf{0.7404}_{0.0003}$	$0.7381_{0.0004}$	$0.6967_{0.0004}$	$0.7060_{0.0006}$	$\mathbf{0.7212}_{0.0006}$
V3	$0.9330_{0.0004}$	$0.9328_{0.0006}$	$\mathbf{0.9384}_{0.0004}$	$0.9480_{0.0003}$	$0.9475_{0.0006}$	$\mathbf{0.9518}_{0.0002}$
avg	**0.8988**	0.8968	0.8958	0.8753	0.8919	**0.8944**

and 1, implement the DAMSDI experiment with bilinarly implanted targets for five times, and report the median AUC for assessing the detection efficacy and the range of AUCs for assessing the stability of result. From Table 5, we see that the training AUCs of DAMSDI may be improved on targets F2, F3, V2 by using different values of u other than 1, but the test AUCs decline at a larger magnitude. Therefore, without any prior knowledge on the target proportion in a pixel, we will use $u = 1$ as the default setting for all experiments in our paper; all reported results on real datasets are generated from the setting that corresponds to the median sum of FARs (for the HyMap dataset) or the median average of AUCs (for the MUUFL dataset). Moreover, the ranges of AUCs are near zero for all targets, indicating that our method is very stable over random synthesis of target-background mixed spectra.

We now further investigate the relationship between the ground-truth implanted fraction f_m and the target proportion γ_n by taking V2 as an example. Although the formulae for implanting targets, i.e. Eq. (23), and for synthesising the target-background mixed spectra, i.e. Eq. (17), are not identical, f_m and γ_n both reflect the amount of target information in a pixel. Table 6 suggests that, when the target-background interaction spectrum occupies a small fraction of the pixel's spectrum, e.g. $f_m = 0.01$, DAMSDI with a small upper bound of the target proportion ($u = 0.2$) achieves a higher AUC than with a large upper

Table 6: Training AUCs of DAMSDI with different upper bounds of target proportions u on detecting bilinearly implanted target V2 with different implanted fractions f_m.

u \ f_m	0.01	0.05	0.2	0.5
0.2	0.6030	0.6749	0.8059	0.8753
0.5	0.5846	0.6655	0.8136	0.8979
1	0.5786	0.6536	0.8036	0.9167

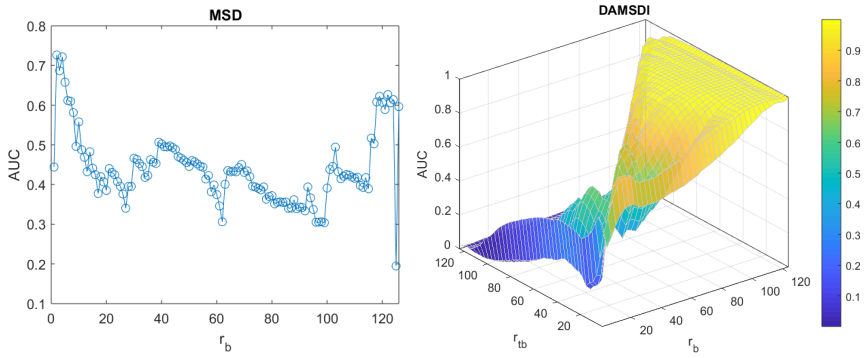

Figure 6: Effects of r_b on MSD and r_b, r_{tb} on DAMSDI for detecting the bilinearly implanted target V2.

bound ($u = 1$). When the interaction spectrum occupies a large fraction, e.g. $f_m = 0.5$, it is preferable to use a large value of u.

Another parameter in the proposed methods is the number of eigenvectors used to construct background and target-background mixed subspaces, i.e. r_b and r_{tb}. In Fig. 6, we present the training AUC of MSD and DAMSDI on detecting the bilinearly implanted target V2 for different values of r_b and r_{tb}. The 3D plot of DAMSDI suggests that, for a large range of r_b and r_{tb} ($r_b \geq 80$), its AUC varies smoothly over consecutive subspace ranks. Comparing the AUC scores between MSD and DAMSDI, we see that, within this range, DAMSDI is always superior to the optimal MSD.

We now examine the constraints on r_b, r_{tb} discussed in Sections 3.1 and 4.1.2; that is $r_b^{\text{DAMSD}}, r_b^{\text{DAMSDI}} \leq r_{b,\text{opt}}^{\text{MSD}}$ and $r_{tb}^{\text{DAMSD}}, r_{tb}^{\text{DAMSDI}} \leq r_{b,\text{opt}}^{\text{MSD}} + 1$. On the one hand, imposing the constraint reduces the search space for the most representative subspaces that gives the largest AUCs, thus reducing the training time. As shown in Table 7, for most targets, the number of pairs to be searched in the constrained case, i.e. $r_{b,\text{opt}}^{\text{MSD}} \times (r_{b,\text{opt}}^{\text{MSD}} + 1)$, is much

Table 7: Effect of constraining r_b and r_{tb} on the training and test AUCs of DAMSDI for bilinearly implanted targets. 'con' and 'unc' represents the method with and without the constraints $r_b^{\text{DAMSDI}} \leq r_{b,\text{opt}}^{\text{MSD}}, r_{tb}^{\text{DAMSDI}} \leq r_{b,\text{opt}}^{\text{MSD}} + 1$, respectively. r_b and r_{tb} list the optimal number of eigenvectors for background and target-background mixed subspaces, respectively.

	training AUCs		test AUCs		$r_{b,\text{opt}}^{\text{MSD}}$	r_b		r_{tb}	
	con	unc	con	unc		con	unc	con	unc
F1	0.9462	1.0000	0.9586	0.9998	11	11	70	6	29
F2	0.7052	0.9999	0.6769	0.9972	5	5	120	1	11
F3	0.9938	1.0000	0.9945	0.9993	16	16	60	6	27
F4	0.9491	0.9999	0.9599	0.9971	11	11	112	6	12
V1	0.9999	0.9999	0.9976	0.9976	125	120	120	10	10
V2	0.7381	0.9999	0.7212	0.9993	2	2	93	3	24
V3	0.9384	0.9999	0.9518	0.9975	11	11	93	6	20
average	0.8958	0.9999	0.8944	0.9983					

smaller than a full search of r_b and r_{tb} over 126×126 pairs. In addition, the constrained methods are less likely to overfit the training data. On the other hand, methods without constraints will detect targets more effectively than the constrained ones since the subspaces with a larger number of eigenvectors could explain spectral variability to a greater extent and hence are more informative. We evaluate the effect of constraining r_b and r_{tb} on the detecting bilinearly implanted targets, and results are listed in Table 7. We see that, without the constraints, DAMSDI achieves near optimal performances in the training stage. Since target spectra are implanted into the same scene in the same manner, there is a high similarity between the training and test data. Therefore, the test performances are almost identical to the training ones for both constrained and unconstrained methods. We will further study the impact of subspace ranks on the MUUFL dataset which contains real training and test data.

4.2. The MUUFL Gulfport dataset

4.2.1. Data description

The second real dataset is the MUUFL dataset, which was collected in November 2010 over the campus of the University of Southern Mississippi – Gulfport, MS, USA [30]. Three hyperspectral images were taken over the same scene at two altitude levels. In this experiment, we use Flight 1 image as the training data and Flight 3 image as the test data since they were collected at same altitude and thus have the same spatial resolution. The image contains 72 spectral bands ranging from 375 to 1050 nm with a 10 nm bandwidth and 325×337 pixels with 1 meter of ground resolution. The first and last four bands are removed due to sensor noise [11]. The RGB image is shown in Fig. 7.

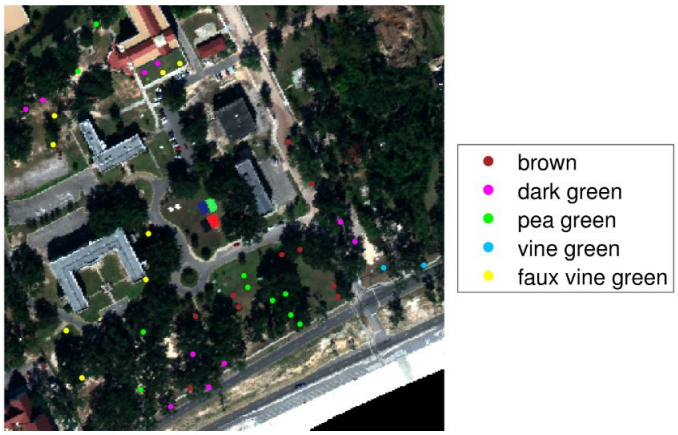

Figure 7: The MUUFL Gulfport dataset in RGB and ground-truth locations of 40 targets marked in different colours.

In this experiment, we select 40 subpixel targets of sizes 0.5m×0.5m and 1m×1m and of five different fabrics: brown (BR) (10 samples), dark green (DG) (10 samples), pea green (PG) (10 samples), vineyard green (VG) (2 samples), faux vineyard green (FVG) (8 samples). The ROI for each target is defined by a 5-by-5 rectangular region centered at the ground-truth location and is shown in Fig. 7. The library spectrum is available for all targets except FVG; we will use the library spectrum of VG as that of FVG, as suggested in [30].

4.2.2. Experimental settings

For the MUUFL dataset, we use the area under the receiver operating characteristic curve (AUC) statistic as the evaluation measure. The reason is as follows. In the HyMap dataset, we calculate the FAR when the single target is correctly identified. In the MUUFL dataset, as each target has multiple samples, we could calculate the FAR when one target sample is detected, two samples are detected, up to all samples are detected. This essentially give the true positive rate and the false positive rate, which are used to plot the ROC curve. Therefore, using AUC would be a more informative criterion for evaluating the detection performance, which is also adopted in [23]. A target detection method is more effective if it has a larger AUC.

The background subspace and the target-background mixed subspace are constructed by following the same procedure as with the HyMap dataset. r_b and r_{tb} are searched under the constraints $r_b^{\text{DAMSD(I)}} \leq r_{b,\text{opt}}^{\text{MSD}}, r_{tb}^{\text{DAMSD(I)}} \leq r_{b,\text{opt}}^{\text{MSD}} + 1$, aiming for the largest AUCs for each target in the training data. The optimal values are listed in Table 8 and will be used to build subspaces in the test stage.

Table 8: Parameters r_b, r_{tb} in subspace-based methods for the MUUFL dataset.

	r_b					r_{tb}	
	OSP	MSD	MSDinter	DAMSD	DAMSDI	DAMSD	DAMSDI
BR	31	15	28	7	7	13	13
DG	32	27	28	20	20	27	27
PG	50	32	38	21	23	17	17
VG	6	4	29	4	4	3	3
FVG	49	19	52	17	15	19	20

4.2.3. Results and discussions

Table 9 lists the AUCs of individual targets and the mean value of AUCs on training and test data. As CEM, AMF and sACE do not learn any parameter and calculate detection score based on the formula and input data, their detection performances in the training and test stages solely depend on the data provided in the particular stage. In other words,

Table 9: Training and test AUCs for the MUUFL Dataset. Best results are in boldface.

Training AUCs

	CEM	AMF	sACE	OSP	MSD	MSDinter	DAMSD	DAMSDI
BR	0.9609	0.9625	0.9783	**0.9912**	0.9873	0.9784	0.9862	0.9846
DG	0.9518	0.9685	0.9585	0.9807	0.9849	0.9798	**0.9941**	0.9937
PG	0.9588	0.9710	0.9486	0.9741	0.9812	0.9815	0.9840	**0.9867**
VG	0.9685	0.9889	0.9761	0.9924	0.9938	0.9990	0.9972	**0.9994**
FVG	0.9290	0.9236	0.9363	0.9714	0.9799	0.9816	**0.9900**	0.9846
average	0.9538	0.9629	0.9596	0.9819	0.9854	0.9841	**0.9903**	0.9898

Test AUCs

	CEM	AMF	sACE	OSP	MSD	MSDinter	DAMSD	DAMSDI
BR	0.9790	0.9732	**0.9826**	0.9639	0.9687	0.9665	0.9753	0.9785
DG	0.9626	0.9614	0.9612	**0.9811**	0.9755	0.9611	0.9746	0.9779
PG	0.9473	0.9491	0.9448	0.9598	0.9679	0.8825	**0.9801**	0.9600
VG	0.9778	0.9765	0.9737	0.9899	0.9882	0.9687	**0.9904**	0.9562
FVG	0.9526	0.9541	**0.9795**	0.9549	0.9457	0.8740	0.9678	0.9622
average	0.9639	0.9684	0.9699	0.9699	0.9692	0.9305	**0.9776**	0.9670

target detection in the training stage and test stage can be viewed as two separate tasks. Therefore, it is possible that the test AUCs of these methods are higher than the training AUCs. OSP, MSD, MSDinter, DAMSD and DAMSDI learn optimal r_b and r_{tb} on the training data and generally they are expected to perform worse on the test data. In the training stage, DAMSD and DAMSDI are both superior to all comparison methods as they achieve higher AUCs on four targets and obtain the best average AUC. In the test stage, DAMSD sustains its superior performance to MSD, in terms of both the number of targets and the average AUC. Same conclusion can be drawn when comparing MSDinter with DAMSDI. This result is again in favor of learning a more representative target-background mixed subspace than concatenating target subspace and background subspace.

Another potential advantage of DA-type methods is that they speed up target detection by avoiding the matrix inversion operation. We record the execution time in the test stage

Table 10: Effect of the target proportion γ_n on the AUCs of DAMSD and DAMSDI for the MUUFL training data. γ_n is selected from $U(0.05, u)$ and three values of u are compared. 'worst' denotes the smallest average of AUCs out of three rounds of experiments.

	DAMSD			DAMSDI		
	$u = 0.2$	$u = 0.5$	$u = 1$	$u = 0.2$	$u = 0.5$	$u = 1$
BR	**0.9881**	0.9862	0.9862	**0.9905**	0.9859	0.9846
DG	**0.9950**	0.9948	0.9941	**0.9944**	0.9937	0.9937
PG	**0.9892**	0.9863	0.9840	**0.9878**	0.9860	0.9867
VG	0.9943	**0.9978**	0.9972	0.9913	0.9988	**0.9994**
FVG	0.9879	0.9871	**0.9900**	**0.9870**	0.9852	0.9846
average	**0.9909**	0.9904	0.9903	**0.9902**	0.9899	0.9898
worst	0.9908	0.9899	0.9897	0.9902	0.9898	0.9897

only since it matters the most in real-time target detection; the target detection algorithm is executed on a computer with Intel Core i5 CPU at 2.4 GHz and 8.0 GB RAM using MATLAB (R2018a). For MSD, MSDinter, DAMSD and DAMSDI, the average execution time to detect one target is 362, 382, 221, 221 ms, respectively.

Next, we investigate the effect of choosing different upper bounds u of the target proportion γ_n on the training performance of DAMSD and DAMSDI. We set $u = 0.2, 0.5, 1$ and run the experiment for three times. Table 10 reports results from the round whose average AUC (mean value of AUCs averaged over five targets) equals to the median of the three average AUCs. It also lists the smallest value of average AUC from three rounds of experiments, denoted as 'worst'. The performance does not change much by using different values of u, indicating that our method is quite insensitive to this parameter. Similarly to the simulation study with the HyMap dataset, we cannot find an optimal value of the upper bound that could give the highest AUC on all targets and hence $u = 1$ is used as the default setting. Comparing the worst average AUC to the median average AUC, we find that their difference is tiny, which suggests that our method is stable over randomly synthesised target-background mixed spectra.

We end this section by investigating the effect of constraining r_b, r_{tb} on training and test

Table 11: Training and test AUCs of DAMSD and DAMSDI with constrained ('con') and unconstrained ('unc') r_b and r_{tb} for the MUUFL data. Values in boldface mean that unconstrained DAMSD and DAMSDI achieves higher AUCs than constrained ones.

	DAMSD				DAMSDI			
	Training AUC		Test AUC		Training AUC		Test AUC	
	con	unc	con	unc	con	unc	con	unc
BR	0.9862	**0.9942**	0.9753	0.9734	0.9846	**0.9930**	0.9785	0.9692
DG	0.9941	0.9941	0.9746	0.9746	0.9937	0.9937	0.9779	0.9779
PG	0.9840	**0.9896**	0.9801	0.9697	0.9867	**0.9906**	0.9600	**0.9724**
VG	0.9972	**0.9990**	0.9904	0.9681	0.9994	0.9994	0.9562	0.9562
FVG	0.9900	0.9900	0.9678	0.9678	0.9846	**0.9909**	0.9622	**0.9754**
average	0.9903	**0.9934**	0.9776	0.9707	0.9898	**0.9935**	0.9670	**0.9702**

performances of DAMSD and DAMSDI; the constraints are $r_b^{\text{DAMSD(I)}} \leq r_{b,\text{opt}}^{\text{MSD}}$, $r_{tb}^{\text{DAMSD(I)}} \leq r_{b,\text{opt}}^{\text{MSD}} + 1$. From Table 11, we see that the unconstrained DA-type methods outperform constrained ones on the training data. However, on the test data, unconstrained DAMSD performs much worse than the constrained one and the benefit of using unconstrained DAMSDI becomes smaller. This could be an indication of model overfitting.

5. Conclusion and future work

This paper proposed two new methods to improve the estimation of target-background mixed subspace used in MSD and MSDinter. We augmented target data in two ways to overcome the scarcity problem of target spectra, learned a target-background mixed subspace which represents mixed target spectra in subpixel target detection problems and reduces the detection time, and then obtained two new subpixel target detectors, namely DAMSD and DAMSDI. Encouraging results on the HyMap and MUUFL datasets suggests that learning a subspace from synthetic target-background mixed data could improve the target detection performance.

While we mix the target spectrum with all background spectra, the target in fact usually only interacts with nearby materials. In our future work, we would add a data preprocessing step prior to the construction of target-background mixed subspace, such as

first identifying the pixels that potentially contain the target and then mixing the target spectrum with the spectra from these pixels and their surrounding pixels. This would allow us to obtain an even more representative target-background mixed subspace. Moreover, it would be valuable to investigate the use of other endmember extraction methods in our future work, especially for non-linearly mixed spectra. Furthermore, as mentioned in Section 1, sparse representation (SR)-based methods require a set of training target samples. Exploring the applicability of data-augmentation methods to SR-based methods would be another interesting future work.

Acknowledgment

This work was partly supported by the Royal Society under Royal Society-Newton Mobility Grant IE161194, and by the National Natural Science Foundation of China under Grant 61711530239.

References

[1] Natural Resources Canada, Hyperspectral imagery for forests, url: https://www.nrcan.gc.ca/forests/measuring-reporting/remote-sensing/13437. Last visited on 18/Mar/2019 (2016).

[2] N. M. Nasrabadi, Hyperspectral target detection: An overview of current and future challenges, IEEE Signal Processing Magazine 31 (1) (2014) 34–44 (2014).

[3] E. J. Kelly, An adaptive detection algorithm, IEEE Transactions on Aerospace and Electronic Systems AES-22 (12) (1986) 115–127 (1986).

[4] J. C. Harsanyi, C.-I. Chang, Hyperspectral image classification and dimensionality reduction: An orthogonal subspace projection approach, IEEE Transactions on Geoscience and Remote Sensing 32 (4) (1994) 779–785 (1994).

[5] D. Manolakis, C. Siracusa, G. Shaw, Adaptive matched subspace detectors for hyperspectral imaging applications, in: 2001 IEEE International Conference on Acoustics, Speech, and Signal Processing. Proceedings, Vol. 5, IEEE, 2001, pp. 3153–3156 (2001).

[6] C.-I. Chang, D. C. Heinz, Constrained subpixel target detection for remotely sensed imagery, IEEE Transactions on Geoscience and Remote Sensing 38 (3) (2000) 1144–1159 (2000).

[7] Z. Wang, J.-H. Xue, The matched subspace detector with interaction effects, Pattern Recognition 68 (2017) 24–37 (2017).

[8] Y. Chen, N. M. Nasrabadi, T. D. Tran, Sparse representation for target detection in hyperspectral imagery, IEEE Journal of Selected Topics in Signal Processing 5 (3) (2011) 629–640 (2011).

[9] Y. Zhang, B. Du, L. Zhang, A sparse representation-based binary hypothesis model for target detection in hyperspectral images, IEEE Transactions on Geoscience and Remote Sensing 53 (3) (2015) 1346–1354 (2015).

[10] T. Wang, B. Du, L. Zhang, An automatic robust iteratively reweighted unstructured detector for hyperspectral imagery, IEEE Journal of Selected Topics in Applied Earth Observations and Remote Sensing 7 (6) (2014) 2367–2382 (2014).

[11] A. Zare, C. Jiao, T. Glenn, Discriminative multiple instance hyperspectral target characterization, IEEE Transactions on Pattern Analysis and Machine Intelligence (2017).

[12] M. O. Smith, P. E. Johnson, J. B. Adams, Quantitative determination of mineral types and abundances from reflectance spectra using principal components analysis, Journal of Geophysical Research: Solid Earth 90 (S02) (1985) C797–C804 (1985).

[13] H. Wendland, Numerical Linear Algebra: An Introduction, Cambridge Texts in Applied Mathematics, Cambridge University Press, 2017 (2017).

[14] D. Manolakis, C. Siracusa, G. Shaw, Hyperspectral subpixel target detection using the linear mixing model, IEEE Transactions on Geoscience and Remote Sensing 39 (7) (2001) 1392–1409 (2001).

[15] R. B. Singer, T. B. McCord, Mars-large scale mixing of bright and dark surface ma-

terials and implications for analysis of spectral reflectance, in: Lunar and Planetary Science Conference Proceedings, Vol. 10, 1979, pp. 1835–1848 (1979).

[16] W. Fan, B. Hu, J. Miller, M. Li, Comparative study between a new nonlinear model and common linear model for analysing laboratory simulated-forest hyperspectral data, International Journal of Remote Sensing 30 (11) (2009) 2951–2962 (2009).

[17] R. Heylen, P. Scheunders, A multilinear mixing model for nonlinear spectral unmixing, IEEE Transactions on Geoscience and Remote Sensing 54 (1) (2016) 240–251 (2016).

[18] R. Heylen, M. Parente, P. Gader, A review of nonlinear hyperspectral unmixing methods, IEEE Journal of Selected Topics in Applied Earth Observations and Remote Sensing 7 (6) (2014) 1844–1868 (2014).

[19] L. Zhang, L. Zhang, D. Tao, X. Huang, B. Du, Hyperspectral remote sensing image subpixel target detection based on supervised metric learning, IEEE Transactions on Geoscience and Remote Sensing 52 (8) (2014) 4955–4965 (2014).

[20] Z. Wang, R. Zhu, K. Fukui, J.-H. Xue, Matched shrunken cone detector (MSCD): Bayesian derivations and case studies for hyperspectral target detection, IEEE Transactions on Image Processing 26 (11) (2017) 5447–5461 (2017).

[21] Z. Wang, J.-H. Xue, Matched shrunken subspace detectors for hyperspectral target detection, Neurocomputing 272 (2018) 226–236 (2018).

[22] X. Yang, L. Zhang, L. Gao, J.-H. Xue, Msdh: Matched subspace detector with heterogeneous noise, Pattern Recognition Letters 125 (2019) 701–707 (2019).

[23] C. Jiao, C. Chen, R. G. McGarvey, S. Bohlman, L. Jiao, A. Zare, Multiple instance hybrid estimator for hyperspectral target characterization and sub-pixel target detection, ISPRS Journal of Photogrammetry and Remote Sensing 146 (2018) 235–250 (2018).

[24] P. Zhong, Z. Gong, J. Shan, Multiple instance learning for multiple diverse hyperspectral target characterizations, IEEE transactions on neural networks and learning systems (2019).

[25] Y. Cohen, D. G. Blumberg, S. R. Rotman, Subpixel hyperspectral target detection using local spectral and spatial information, Journal of Applied Remote Sensing 6 (1) (2012) 1 – 16 (2012).

[26] D. Snyder, J. Kerekes, I. Fairweather, R. Crabtree, J. Shive, S. Hager, Development of a web-based application to evaluate target finding algorithms, in: IEEE International Geoscience and Remote Sensing Symposium, Vol. 2, IEEE, 2008, pp. II–915 (2008).

[27] A. P. Cisz, J. R. Schott, Performance comparison of hyperspectral target detection algorithms in altitude varying scenes, in: Algorithms and Technologies for Multispectral, Hyperspectral, and Ultraspectral Imagery XI, Vol. 5806, International Society for Optics and Photonics, 2005, pp. 839–849 (2005).

[28] L. Gao, B. Yang, Q. Du, B. Zhang, Adjusted spectral matched filter for target detection in hyperspectral imagery, Remote Sensing 7 (6) (2015) 6611–6634 (2015).

[29] B. Du, L. Zhang, Target detection based on a dynamic subspace, Pattern Recognition 47 (1) (2014) 344–358 (2014).

[30] P. Gader, A. Zare, R. Close, J. Aitken, G. Tuell, Muufl gulfport hyperspectral and lidar airborne data set, Univ. Florida, Gainesville, FL, USA, Tech. Rep. REP-2013-570 (2013).